Dalton Transactions

ROYAL SOCIETY OF CHEMISTRY

PAPER

View Article Online
View Journal | View Issue

Cite this: *Dalton Trans.*, 2025, **54**, 11225

Complementary effect of co-doping Mn and B in Fe–N–C single-atom catalysts on enhancing the oxygen reduction reaction performance†

Jiansheng Liu,‡ Lili Cao,‡ Haoran Ma, Qiyue Jia, Jianing Ma and Zhanli Chai *

Received 29th April 2025,
Accepted 18th June 2025

DOI: 10.1039/d5dt01001b

rsc.li/dalton

With more flexible active sites and tunable electronic structures, electrocatalysts constructed based on doping have emerged as a frontier in various catalytic reactions. However, the mechanisms of some co-doped catalysts for the improved performance remain unclear. Herein, we report a distinctive Fe–N–C single-atom catalyst (SAC) co-doped with Mn and B, which displayed excellent oxygen reduction reaction (ORR) performance in an alkaline electrolyte, with a higher half-wave potential of 0.85 V, a lower Tafel slope (61.79 mV dec^{-1}), a larger kinetic current density (3.4 mA cm^{-2}) and a better durability than Fe-NC and Fe-BNC catalysts. Studies on the structure–activity relationship indicated that the co-doping of Mn compensated for the structural issues such as structural distortion, lattice shrinkage, increased defects, and reduction of M–N active sites caused by B doping. It also compensated for performance defects such as slow ORR kinetics, poor electrical conductivity, low selectivity, and weak stability. Consequently, this work validates the immense potential of metal and non-metal co-doped Fe–N–C SACs as active and sustainable ORR catalysts.

1. Introduction

Proton exchange membrane fuel cells (PEMFCs) are electrochemical devices that use hydrogen as the fuel and produce water as the reaction product. During this process, as no other pollutants are generated, they are considered clean and energy-efficient sources.[1] In PEMFCs, the oxygen reduction reaction (ORR) at the cathode is the rate-determining-step of the reaction because the ORR involves multiple steps, such as the adsorption and transfer of O_2, O═O bond breaking, and desorption of the product H_2O.[2] The Pt/C catalyst is currently a commercially available catalyst for the ORR. However, owing to its high cost and limited reserves, the development of highly efficient non-precious metal catalysts for ORR has become a hot research topic.[3,4] So far, it has been found that the catalysts with an M–N–C configuration are highly desirable in the field of ORR.[5,6] Although inherent differences result from the type of metal atoms present in an M–N–C catalyst, the electronic structure of the active sites is mainly regulated by the coordinating atoms N and C.[7] Moreover, different coordination numbers and configurations can alter the electronic structure of the central atom, and there is a possibility to realize high catalytic activity, which is comparable to that of the commercial Pt/C catalyst.[8] Nevertheless, the poor stability of M–N–C SAC catalyst remains a big challenge that needs to be solved urgently.[9]

Among M–N–C catalysts, the Fe–N–C single-atom catalysts (SACs) boast the best ORR activity.[10] This is because they can evenly distribute metal atoms on the carbon carrier, thus avoiding metal–atom aggregation.[11] Additionally, the metal atoms combine with the doped N atoms to form Fe–N_4, which can effectively enhance the oxygen reduction reaction.[12] However, traditional Fe–N–C catalysts exhibit poor durability during the ORR process.[13] Doping a second metal M into Fe–N–C can provide dual-metal active sites, thereby improving the catalyst's activity.[14] Meanwhile, the strong bonding effect of the doped metal can anchor the Fe–N_4 structure and inhibit the agglomeration or leaching of Fe atoms, thus enhancing the ORR catalytic stability.[15] Besides, the doping of non-noble metals can effectively improve the stability of Fe–N–C SACs.[16] Apart from using N to anchor and adjust the electronic structure of metal atoms, elements such as S, P, and B are commonly used for doping to further enhance the catalytic performance of Fe–N–C SACs.[17] Among them, the doping of boron atoms can increase the spin density of the graphene plane or enhance the electron transfer, thereby improving the ORR activity and durability.[18] At present, there are reports on the modification of Fe–N–C SACs using the strategy of co-doping with metals and non-metals,[19] but the synergistic

Inner Mongolia Key Laboratory of Rare Earth Catalysis, School of Chemistry and Chemical Engineering, Inner Mongolia University, Hohhot 010021, PR China. E-mail: chaizhanli@imu.edu.cn

†Electronic supplementary information (ESI) available. See DOI: https://doi.org/10.1039/d5dt01001b

‡These authors contributed equally to this work.

mechanism between metal and non-metal co-doping remains unclear.

Herein, we used melamine foam as the substrate and synthesized an Mn- and B-co-doped Fe–N–C (Fe/Mn-BNC) SAC through an impregnation followed by calcination method. The comparative catalysts (Fe-NC and Fe-BNC SACs) were prepared separately using the same approach. The structures and chemical states of the three catalysts were further explored, which indicated that single-atomic Fe and Mn were distributed on the reduced and N/B co-doped graphene oxide layer. Subsequently, the ORR electrocatalytic performance of the different electrocatalysts was investigated and compared with the commercial Pt/C. It was found that the activity and stability of the Fe/Mn-BNC catalyst were significantly improved through the complementary modification of Mn and B dual-doping.

2. Experimental

2.1 Materials

Ferric nitrate nonahydrate ($Fe(NO_3)_3{\cdot}9H_2O$, 98.5%), manganese(II) chloride ($MnCl_2{\cdot}4H_2O$, 99%), boric acid (H_3BO_3, 99%), urea (CH_4N_2O, 98.5%) and polyethylene glycol (PEG-2000, 98.5%) were purchased from Beijing Innochem. All the employed chemicals were of analytical grade and were used directly without additional purification.

2.2 Synthesis of catalysts

0.009 g of $Fe(NO_3)_3{\cdot}9H_2O$, 0.009 g of $MnCl_2{\cdot}4H_2O$, 0.5 g of polyethylene glycol (PEG-2000), 5.0 g of urea, and 0.15 g of boric acid were added to 100 mL of deionized water and stirred for 30 min. The melamine foam was then immersed in the resulting homogeneous solution. After 24 h, the melamine foam was gently squeezed to remove the excess solution and then dried at 80 °C for 12 h. Subsequently, the dried melamine foam was heated at 900 °C under an Ar atmosphere for 6 h. Finally, the catalyst was washed several times with a mixture of deionized water and absolute ethanol and was dried to obtain the Mn and B co-doped Fe–N–C single-atom catalyst (denoted as Fe/Mn-BNC). The comparative catalyst Fe-BNC was obtained by removing $MnCl_2{\cdot}4H_2O$ from the precursor and following the above reaction process. Additionally, Fe-NC was prepared by removing both $MnCl_2{\cdot}4H_2O$ and boric acid from the precursor and following the same approach.

2.3 Characterizations

Powder X-ray diffraction (XRD) experiments were conducted using a PANalytical Empyrean diffractometer. The instrument was operated at 40 kV and 40 mA with a Cu K_α radiation (λ = 0.154 nm). Scanning electron microscope (SEM) analysis was carried out using a Hitachi S-4800 operated at 10 kV, while transmission electron microscope (TEM) observations were performed using an FEI Tecnai G2 F20 S-TWIN at 200 kV. X-ray photoelectron spectroscopy (XPS) data were collected using an AXIS-ULTRA DLD (Kratos Analytical Ltd) instrument, with the binding energy of the C 1s peak at 284.60 eV used as the reference. Raman spectra were obtained using a Horiba HR Evolution Raman spectrometer with an excitation source of 514 nm. Electrochemical measurements were carried out using an electrochemical workstation (AutoLab, PGSTAT 302N).

2.4 Electrochemical measurements

A PGSTAT302N AutoLab electrochemical workstation was utilized to perform cyclic voltammetry (CV) measurements and to apply rotating disk electrode (RDE, RRDE-3A) techniques. The synthesized catalysts were deposited on a glassy carbon RDE with a diameter of 3.0 mm. A Pt wire and an Ag|AgCl electrode were used as the counter and reference electrodes, respectively. The fabrication process of the working electrode was as follows: 5.0 mg of the catalyst was dispersed in 10 μL of Nafion (5 wt%) and 100 μL of ethanol. The mixture was stirred in an ambient temperature until a uniform ink was formed. Subsequently, 3.2 μL of the ink was precisely dropped onto the disk surface of the pre-polished glassy carbon electrode. The oxygen reduction reaction (ORR) properties were investigated using CV in an O_2-saturated 0.1 M KOH solution at room temperature, with a scan rate of 100 mV s^{-1}. The durability of the catalysts was assessed *via* an accelerated durability test (ADT). The ADT test parameters included a scanning rate of 50 mV s^{-1}, a voltage range of 0.4–1.1 V (*vs.* RHE), and a total of 6000 cycles of CV testing. After every 2000 cycles, an LSV test was conducted to observe the changes in the half-wave potential and the limiting diffusion current. During the methanol tolerance test, current–time (I–t) measurements were carried out at a constant potential of 0.84 V and a rotation speed of 1600 rpm for a duration of 800 s. At 300 s, 5 mL methanol (3 M) was subsequently added to the electrolyte. The kinetic current density of the catalysts was computed based on the Koutecky–Levich (K–L) equation.

$$\frac{1}{J}=\frac{1}{J_L}+\frac{1}{J_K}$$

J refers to the current measured using the cyclic voltammetry (CV) method, J_L indicates the limiting diffusion current and J_K represents the kinetic current.

3. Results and discussion

Fig. 1 illustrates a schematic of the synthesis process of the Fe/Mn-BNC catalyst, using $Fe(NO_3)_3{\cdot}9H_2O$ and $MnCl_2{\cdot}4H_2O$ as the metal sources, urea as the nitrogen source, boric acid for B doping, and melamine foam as the carbon substrate. Initially, various raw materials were dissolved in water and mixed into a homogeneous solution. Subsequently, the melamine foam was immersed into it, and the metal ions, urea, and boric acid were fully embedded in the three-dimensional (3D) porous structure of melamine. After 24 h, the saturated 3D melamine foam was dried to obtain the precursor, which was then heated to 900 °C at a rate of 3 °C min^{-1} under an Ar atmosphere and maintained for 6 h. Under these conditions of

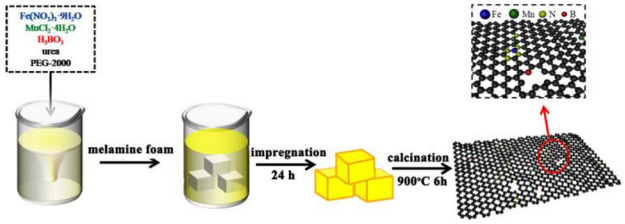

Fig. 1 Schematic of the synthesis process of Fe/Mn-BNC.

high temperature and protective gas, the N element decomposed from urea and the B element decomposed from boric acid were doped onto the graphene structure formed by the melamine foam to obtain the BNC carbon substrate.[20] Meanwhile, Fe and Mn atoms produced by the pyrolytic reduction of the metal salts were doped into the BNC carrier, thus forming Fe/Mn-BNC.[21] By changing the metal sources and the boron source, two comparative catalysts were obtained, namely Fe-NC and Fe-BNC.

Fig. 2 presents the SEM images, TEM images and EDS patterns of Fe-NC, Fe-BNC and Fe/Mn-BNC. Comparing Fig. $2a_1$ with Fig. $2b_1$, it was clear that the doping of B led to the collapse of the 3D structure of the melamine foam, resulting in the formation of a lamellar fragment structure. Alternatively, when Fe–N–C was co-doped with B and Mn (Fig. $2c_1$), the 3D framework structure was well preserved. Moreover, the surface of Fe/Mn-BNC was rougher than that of Fe-NC, indicating that the simultaneous existence of Fe, Mn, and B was beneficial for the formation of a 3D porous framework structure with a relatively large specific surface area. This was the result of the structural compensation effect between Mn and B co-doping, which facilitated the electron transfer.[22] From the TEM image of Fe-NC in Fig. $2a_2$, the graphene layer and graphitization can be observed. Fig. $2b_2$ shows that the graphene sheets are stacked together in the Fe-BNC sample, which are thinner than those in Fe-NC; the "fingerprint" structure of the graphene can be observed in the HRTEM inset image. As observed in the TEM image of Fe/Mn-BNC (Fig. $2c_2$), their graphene sheets were the thinnest, with the greatest number of wrinkles and the highest degree of graphitization. Moreover, no lattice fringes ascribed to the metal were observed, which preliminarily demonstrated that the metal in the catalyst might exist in the form of single atoms. Energy-dispersive spectroscopy (EDS) was used to measure the compositions of the three samples, and the results are shown in Fig. $2a_3$, b_3, and c_3. The Cu signal was the substrate signal of the copper mesh used for TEM sample preparation. As shown in Fig. $2a_3$, only three elements (Fe, N, and C) existed in Fe-NC, and the content of Fe was 0.03 at%. In addition to Fe, N, and C, the elemental signal for B (2.28 at%) was detected in Fe-BNC, and the content of Fe was also 0.03 at% (Fig. $2b_3$). In Fe/Mn-BNC, in addition to Fe, N, C, and B, the elemental signal of Mn (0.09 at%) was detected, and the content of Fe was 0.09 at% (Fig. $2c_3$). Moreover, as observed from the ICP-AES data (Table S2†), metallic elements with a content of around 0.15 wt% were detected in Fe-NC, Fe-BNC and Fe/Mn-BNC samples. Therefore, it was inferred that trace metals could be detected in the carbon substrate of the three catalysts.

From the TEM image in Fig. 3a, it can be clearly observed that Fe/Mn-BNC exhibited an obvious two-dimensional graphene structure with a wrinkled and porous surface. The fingerprint-like fringes of graphene can be distinctly seen in the HRTEM image (Fig. 3b). Compared with Fe-NC and Fe-BNC in Fig. 2, Fe/Mn-BNC showed a higher graphitization, demonstrating that the simultaneous doping of B and Mn greatly improved the graphitization degree and reduced the thickness of the graphene, which was more conducive to the exposure of metal SAC active sites. To reveal the specific distribution status of Fe and Mn species, aberration-corrected high-angle annular dark-field scanning TEM (HAADF-STEM) images were collected (Fig. 3c), from which an unavoidable Fe and Mn single-atom site could be observed. To further determine the distribution status of the different doped atoms in Fe/Mn-BNC, elemental mapping analysis (STEM mapping) was conducted. In the STEM image shown in Fig. 3d, no obvious metal particles

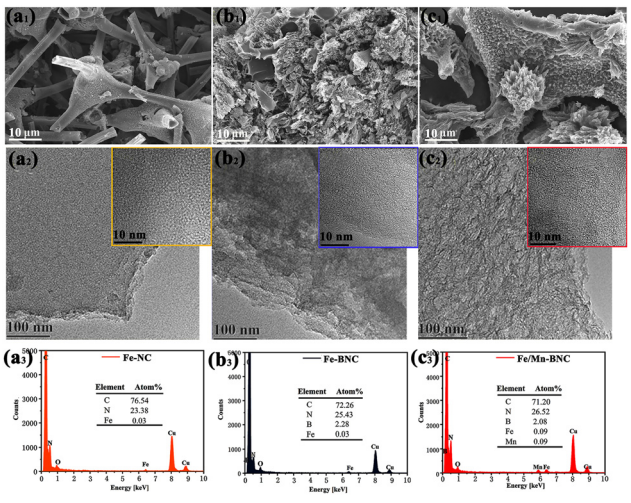

Fig. 2 SEM images, TEM images, EDS patterns of (a_1–a_3) Fe-NC, (b_1–b_3) Fe-BNC, and (c_1–c_3) Fe/Mn-BNC. Insets of a_2–c_2: corresponding HRTEM images.

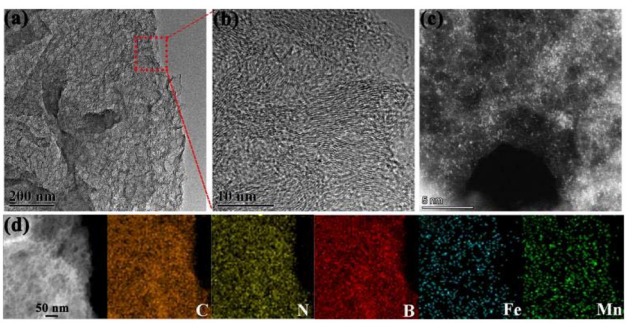

Fig. 3 (a) TEM image, (b) HRTEM image, (c) HADDF-STEM image, and (d) STEM elemental mappings of Fe/Mn-BNC.

could be seen on the graphene, and five elements (C, N, B, Fe, and Mn) were uniformly distributed throughout the graphene region, indicating that both Fe and Mn were distributed on the graphene sheets in the form of single atoms.

Fig. 4a shows the XRD patterns of Fe-NC, Fe-BNC, and Fe/Mn-BNC. All the three samples exhibited two wide peaks at 26.5° and 42.5°, which were attributed to the (100) and (002) planes of reduced graphene oxide (rGO), respectively.[23] There were no obvious peaks of metals or metal compounds in the samples, which may be due to the formation of single metal atoms. When B was doped into Fe-NC (Fe-BNC), the peak at 2θ = 26.5°, belonging to the (100) crystal plane of graphene, shifted to a higher angle, which was mainly attributed to the lattice contraction caused by the substitution of C with B atoms of smaller size.[24] Comparing the XRD peaks of Fe-BNC with Fe/Mn-BNC, it was found that the peak at 2θ = 26.5° shifted significantly to the left and approached the peak of the undoped Fe-NC. This was because Mn ions with a larger size than Fe ions were doped into the graphene substrate, effectively alleviating the lattice contraction caused by B doping. Thus, the lattice compensation between Mn and B might be the main reason for the preserved 3D framework structure of Fe/Mn-BNC. In the Raman spectra in Fig. 4b, the peaks at 1347 cm^{-1} and 1587 cm^{-1} were attributed to the D band and G band of rGO, respectively, further indicating that the prepared carbon existed in the form of graphene. Usually, the I_D/I_G value is used to reflect the degree of defects in graphene.[25] According to the Raman spectra, the I_D/I_G values of Fe-NC, Fe-BNC, and Fe/Mn-BNC were 1.02, 1.18 and 1.07, respectively. Therefore, the doping of B in the carbon substrate created obvious defects, while after the co-doping of Mn and B, the defect compensation significantly enhanced the graphitization, thus contributing to the electron transfer.

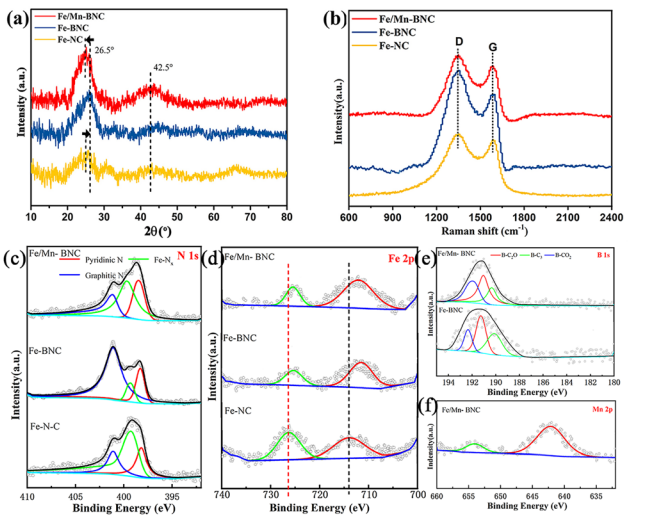

Fig. 4 (a) XRD patterns, (b) Raman spectra, XPS spectra and peak splitting of (c) N 1s, (d) Fe 2p, (e) B 1s, and (f) Mn 2p for Fe-NC, Fe-BNC, and Fe/Mn-BNC.

To further explore the composition and elemental valence states of the catalysts, comparative XPS analyses of Fe-NC, Fe-BNC, and Fe/Mn-BNC were carried out. The full XPS spectra are shown in Fig. S1,† and the elemental binding energies and the proportions of each valence state obtained according to the XPS spectra of different catalysts are listed in Table S1.† The C 1s XPS spectra are shown in Fig. S2,† which indicate that the peaks of the three samples do not differ significantly. In Fig. 4c, the N 1s orbital of each catalyst shows three binding energy peaks at 401.2 eV, 399.6 eV, and 398.5 eV, which can be attributed to the graphitic nitrogen, Fe–N_x bonds, and pyridinic nitrogen, respectively.[26] Notably, the proportion of graphitic nitrogen in Fe-BNC was as high as 68.2%, while the content of Fe–N was as low as 9.1%, indicating that B doping can increase the content of graphitic N but can reduce the Fe–N proportion. Compared with Fe-NC and Fe-BNC, Fe/Mn-BNC exhibited a higher proportion of pyridinic nitrogen (36.1%), which promoted the O–O bond breaking and increased the current density around the carbon atoms, the spin density, and the π-orbitals near the Fermi level, thus improving the oxygen reduction ability of the catalyst.[16] As seen in Fig. 4d, the XPS characteristic peaks of Fe were present in all the three catalysts, and the characteristic peak of Fe clearly shifted to a higher binding energy from Fe-NC to Fe-BNC and then to Fe/Mn-BNC, indicating that doping effectively accelerated the electron transfer from Fe active sites to the carbon substrate.[27] As shown in the B 1s XPS spectra in Fig. 4e, the peaks of B in each catalyst at 190.28 eV, 191.33 eV, and 192.33 eV were attributed to B–C_3, B-C_2O, and B-CO_2, respectively, indicating that the doped B mainly substituted for C.[28] After further doping with Mn, the signal of B on the surface of Fe/Mn-BNC increased significantly. The characteristic peak of Mn in Fe/Mn-BNC was clearly visible in Fig. 4f, indicating that Mn was effectively doped into the Fe-BNC substrate. Combining the above results, Mn co-doping compensated the Fe/Mn–N proportion, which were the main active sites for the ORR process.

Fig. 5a shows the cyclic voltammetry (CV) curves of Fe-NC, Fe-BNC and Fe/Mn-BNC under two atmospheres, including the dashed line measured under a saturated N_2 condition and the solid line tested under a saturated O_2 condition. The electrolyte solution used for all the three catalysts was a 0.1 M KOH solution. Under the O_2 condition (the solid lines), the three catalysts exhibited a downward oxygen reduction peak, indicating that all the catalysts showed a catalytic response to the oxygen reduction reaction (ORR). Fig. 5b shows the linear sweep voltammetry (LSV) curves of the three synthesized catalysts and commercial Pt/C measured in an O_2-saturated 0.1 M KOH solution. These curves demonstrated that the magnitude of the half-wave potentials ($E_{1/2}$) of the four catalysts followed the order of commercial Pt/C (0.87 V) > Fe/Mn-BNC (0.85 V) > Fe-BNC (0.83 V) > Fe-NC (0.82 V). Compared with Fe-NC and Fe-BNC, Fe/Mn-BNC offered an enhanced ORR activity. Furthermore, by comparison, the catalytic performance of Fe/Mn-BNC was still competitive with other non-precious metal electrocatalysts reported to date. More details are listed in Table S3,† implying that the co-doping of Mn and B could sig-

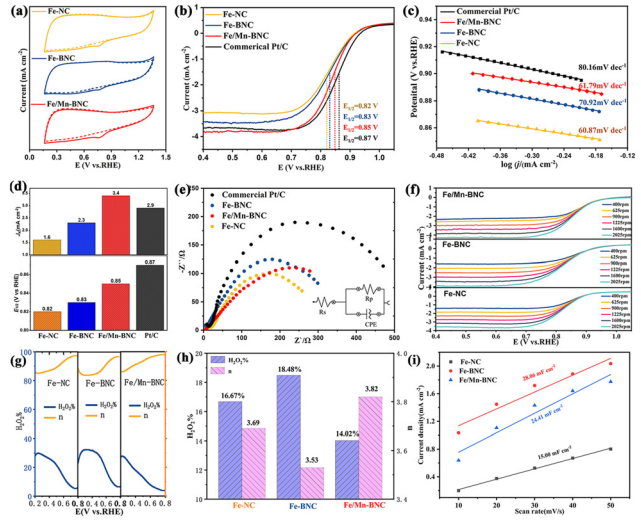

Fig. 5 (a) CV curves, (b) LSV curves, (c) Tafel curves, (d) comparison of $E_{1/2}$ and kinetic current density (J_K), (e) EIS Nyquist plots and fitting circuit of Fe-NC, Fe-BNC, Fe/Mn-BNC and Pt/C, (f) LSV curves at different rotating speeds, (g) H_2O_2% and number of electron transfers (n) *vs.* potential, (h) comparison of average H_2O_2% and n, and (i) C_{dl} slopes of Fe-NC, Fe-BNC, and Fe/Mn-BNC in 0.1 M KOH.

nificantly increase the active sites for the oxygen reduction reaction.[29] As seen in Fig. S3,† the half-wave potentials of Fe/Mn-BNC with mass ratios of Fe/Mn of 1 : 2 and 2 : 1 were 0.81 V and 0.82 V, respectively, which were lower than that of Fe/Mn-BNC (0.85 V, 1 : 1). Besides, the half-wave potentials of the catalysts with lower (1.5 wt%) and higher (6 wt%) dosages of B were 0.82 V and 0.83 V, respectively. To further observe the ORR kinetic process, the Tafel slope was calculated using the LSV curves, as shown in Fig. 5c. In a 0.1 M KOH solution, the Tafel slopes of Fe-NC, Fe-BNC, and Fe/Mn-BNC were 60.87 mV dec^{-1}, 70.92 mV dec^{-1}, and 61.79 mV dec^{-1}, respectively, all of which were lower than that of commercial Pt/C (80.16 mV dec^{-1}). The above results showed that boron (B)-doping in Fe-NC slowed down the ORR kinetics owing to the excessive defects. With the synergistic doping of manganese (Mn), the reaction kinetics was well compensated, thus improving the catalytic activity. As presented in Fig. 5d, the original Fe-NC provided a lower kinetic current density (J_K) of 1.6 mA cm^{-2}. In contrast, the Fe/Mn-BNC exhibited a more remarkable performance improvement with a J_K of 3.4 mA cm^{-2}, surpassing those of Fe-BNC (2.3 mA cm^{-2}) and Pt/C (2.9 mA cm^{-2}), further verifying the improved ORR kinetics with B and Mn co-doping. To directly compare the electron/charge transport characteristics during ORR catalysis, electrochemical impedance spectroscopy (EIS) was recorded for all the four samples (Fig. 5e). The impedance values of the three as-obtained samples were in the range of 300–400 Ω, which was smaller than that of Pt/C (~500 Ω), indicating their high electrical conductivity. Obviously, compared with the original Fe-NC, the doping of B (Fe-BNC) led to a decrease in the electrical conductivity due to the defects, while the co-doping of Mn (Fe/Mn-BNC) improved the overall electrical conductivity of the material. To explore the kinetic electron transfer pathway of the oxygen reduction reaction, a rotating ring-disk electrode was used to test the electron transfer numbers and hydrogen peroxide (H_2O_2) yields. Fig. 5f shows the LSV curves at different rotating rates of the three catalysts, which demonstrated that the limiting currents exhibited a linear relationship with the rotational speeds, indicating that all the three catalysts followed a diffusion-controlled ORR process. Based on the results provided in Fig. 5f and using the Koutecky–Levich (K–L) equation, the electron transfer numbers (n) and the H_2O_2 yields were calculated and shown in Fig. 5g and h. Fe-BNC exhibited a lower n (3.53) than Fe-NC (3.69), and the H_2O_2 yield of Fe-BNC (18.48%) was higher than that of Fe-NC (16.67%). This was mainly because the doped B sites showed a greater preference for the stable *OOH intermediate and were conducive to the $2e^-$ electron transfer path.[30] In comparison, Fe/Mn-BNC possessed the highest n (3.82) and the lowest H_2O_2 yield (14.02%), implying that the co-doping of Mn efficiently compensated for the decrease in the ORR selectivity caused by B doping, and the highest $4e^-$ ORR selectivity was achieved through the synergy between Mn and B co-doping. The double-layer capacitance can reflect the number of intrinsic active sites of a catalyst. CV testing (Fig. S4, ESI†) was conducted to analyze the C_{dl} of Fe-NC, Fe-BNC, and Fe/Mn-BNC. As shown in Fig. 5i, Fe/Mn-BNC (28.06 mF cm^{-2}) exhibited a higher C_{dl} than Fe-NC (24.41 mF cm^{-2}) and Fe-BNC (15.00 mF cm^{-2}), indicating that Fe/Mn-BNC possessed a greater number of active sites.

The essential factor for evaluating the commercial viability of a catalyst is its durability.[31] To this end, an accelerated deterioration test (ADT) was employed. Fig. 6a, b, and c show the ADT tests of Fe-NC, Fe-BNC and Fe/Mn-BNC, and Fig. 6d shows the LSV curves of three catalysts before and after the ADT. After 6000 consecutive cycles of testing, the half-wave potentials of Fe-NC, Fe-BNC, and Fe/Mn-BNC decreased by 19 mV, 13 mV, and 8 mV, respectively, and their limiting diffusion currents were reduced by 21.6%, 18.1% and 5.0%,

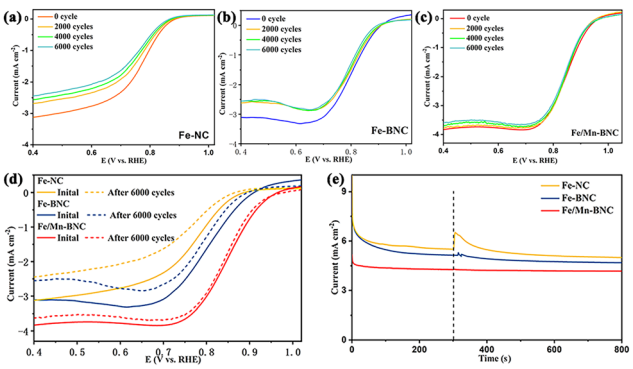

Fig. 6 LSV curves of (a) Fe-NC, (b) Fe-BNC, and (c) Fe/Mn-BNC after durability tests for 0, 2000, 4000, and 6000 cycles, respectively, (d) comparison of ADT curves and (e) I–t curves for anti-methanol poisoning of the three catalysts.

respectively. This indicated that Fe/Mn-BNC has the best durability among the three catalysts. The methanol tolerance testing in ORR ensure the catalyst's selectivity for oxygen reduction without interference from methanol oxidation reactions. As shown in Fig. 6e, a methanol poisoning resistance experiment was conducted using chronoamperometry curves. 3 mL of methanol was added when the time reached 300 s. It was found that Fe/Mn-BNC rarely underwent any charge transfer, while Fe-NC and Fe-BNC successively experienced charge transfers to varying degrees. In comparison, Fe-NC without the doping of B and Mn elements exhibited the largest charge transfer. Therefore, the addition of Mn and B elements improved the methanol tolerance of Fe-NC to different extents. The results in Fig. 6 indicated that the structural changes caused by high defects in Fe-BNC led to a reduction in the ORR active sites, resulting in an unsatisfactory durability.[32] Under the compensation effect between the co-doped Mn and B in Fe/Mn-BNC, the structural stability was improved, the ORR kinetics was accelerated, and the poisoning resistance was enhanced, thus bringing about the best ORR cycle stability.

The density functional theory (DFT) calculation was carried out to explain the improved ORR performance of Fe/Mn-BNC. Fig. 7a shows an optimized structure of Fe/Mn-BNC, in which N and B substitute for C in graphite, and Fe and Mn are connected with N to form M–N active sites. Density of states (DOS) was calculated to analyse the electronic structure of Fe/Mn-BNC (Fig. 7b). Fe/Mn-BNC showed fast electron transfer owing to the narrow bandgap. The surface DOS near the Fermi level (E_f) primarily derived from the highly active Fe and BNC orbitals, which implied that both Fe center and B-NC served as active sites in the ORR process. As shown in Fig. 7c, the free energy profiles indicated that it was more energetically stable to proceed from the *OOH intermediate to H_2O ($4e^-$ pathway) than to H_2O_2 ($2e^-$ pathway). During the ORR process, *H was initially adsorbed onto the surface to form HOOH. This step was endothermic for both TS1 and TS2, but the energy cost for TS2 (0.60 eV) was much lower than that for TS1 (0.80 eV). The subsequent steps for H_2O and H_2O_2 formation were strongly exothermic. For the $4e^-$ ORR pathway, the free energy barrier (ΔG_a) between the transition state and $*H_2O$ was 1.03 eV, which was 0.09 eV higher than that of the $2e^-$ ORR pathway. This clearly indicated that the $4e^-$ ORR activity and selectivity on Fe/Mn-BNC are higher than those of the $2e^-$ ORR.

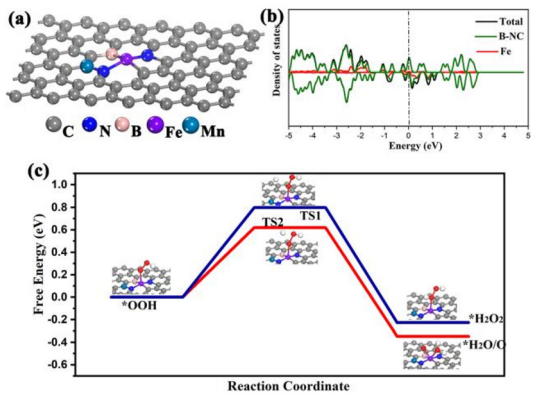

Fig. 7 (a) Optimized structure, (b) DOS, and (c) free energy profiles at 0 V *vs.* SHE for the $2e^-$ and $4e^-$ reaction paths of Fe/Mn-BNC.

4. Conclusions

In summary, Fe-NC, Fe-BNC, and Fe/Mn-BNC were obtained through the method of calcination after impregnation with melamine foam. Structural analysis showed that the co-doping of Mn compensated for the structural distortion, lattice shrinkage, increased defects, and reduction of M–N sites caused by B doping. In the ORR process under alkaline conditions, Fe/Mn-BNC exhibited a superior ORR performance compared with Fe-NC and Fe-BNC, including a higher half-wave potential (0.85 V), a lower Tafel slope (61.79 mV dec^{-1}), a larger kinetic current density (3.4 mA cm^{-2}), a higher number of electron transfer (n = 3.82), and better durability. The enhanced ORR activity and durability of Fe/Mn-BNC mainly stemmed from the compensation effects between co-doped Mn and B on ORR kinetics, electrical conductivity, selectivity, and stability. Our findings demonstrate that the co-doping of metal and non-metal elements can complementarily engineer the electrocatalytic ORR activity, paving a path toward the rational design and development of Fe–N–C SACs as active and sustainable ORR catalysts.

Author contributions

Jiansheng Liu: conceptualization, data curation, formal analysis, methodology, writing – original draft. Lili Cao: conceptualization, data curation, formal analysis, writing – original draft. Haoran Ma: writing – review & editing. Qiyue Jia: writing – original draft. Jianing Ma: investigation, validation. Zhanli Chai: writing – review & editing, funding acquisition.

Conflicts of interest

There are no conflicts to declare.

Data availability

All the relevant data are within the manuscript and its additional files.

Acknowledgements

This work was supported by the Program for Young Talents of Science and Technology in Universities of Inner Mongolia Autonomous Region (NJYT23036), the National Natural Science Foundation of Inner Mongolia (grants

2024LHMS02001), and the Major Basic Research and Open Project of the Inner Mongolia Autonomous Region (30500-515330303). We thank the Electron Microscopy Centre of Inner Mongolia University for the microscopy and microanalysis of our specimens.

References

1 M. Lefevre, E. Proietti, F. Jaouen and J.-P. Dodelet, *Science*, 2009, **324**, 71–74.
2 H. T. Chung, D. A. Cullen, D. Higgins, B. T. Sneed, E. F. Holby, K. L. More and P. Zelenay, *Science*, 2017, **357**, 479–484.
3 M. Zhou, C. Li and J. Fang, *Chem. Rev.*, 2021, **121**, 736–795.
4 G. Liu, A. J. Shih, H. Deng, K. Ojha, X. Chen, M. Luo, I. T. McCrum, M. T. M. Koper, J. Greeley and Z. Zeng, *Nature*, 2024, **626**, 1005–1010.
5 W.-J. Jiang, L. Gu, L. Li, Y. Zhang, X. Zhang, L.-J. Zhang, J.-Q. Wang, J.-S. Hu, Z. Wei and L.-J. Wan, *J. Am. Chem. Soc.*, 2016, **138**, 3570–3578.
6 X. Wan, X. Liu, Y. Li, R. Yu, L. Zheng, W. Yan, H. Wang, M. Xu and J. Shui, *Nat. Catal.*, 2019, **2**, 259–268.
7 A. Han, W. Sun, X. Wan, D. Cai, X. Wang, F. Li, J. Shui and D. Wang, *Angew. Chem., Int. Ed.*, 2023, **62**, e202303185.
8 P.-P. Guo, C. Xu, K.-Z. Yang, C. Lu, P.-J. Wei, Q.-Z. Ren and J.-G. Liu, *Dalton Trans.*, 2024, **53**, 7605–7610.
9 M. Tang, J. Shen, Y. Wang, Y. Zhao, T. Gan, X. Zheng, D. Wang, B. Han and Z. Liu, *Nat. Commun.*, 2024, **15**, 5630.
10 G. Chen, Y. An, S. Liu, F. Sun, H. Qi, H. Wu, Y. He, P. Liu, R. Shi, J. Zhang, A. Kuc, U. Kaiser, T. Zhang, T. Heine, G. Wu and X. Feng, *Energy Environ. Sci.*, 2022, **15**, 2619–2628.
11 A. Morankar, S. Deshpande, Z. Zeng, P. Atanassov and J. Greeley, *Proc. Natl. Acad. Sci. U. S. A.*, 2023, **120**, e2308458120.
12 F. Liu, D. Zhang, F. She, Z. Yu, L. Lai, H. Li, L. Wei and Y. Chen, *ACS Catal.*, 2024, **14**, 9176–9187.
13 Y. Zeng, C. Li, B. Li, J. Liang, M. J. Zachman, D. A. Cullen, R. P. Hermann, E. E. Alp, B. Lavina, S. Karakalos, M. Lucero, B. Zhang, M. Wang, Z. Feng, G. Wang, J. Xie, D. J. Myers, J.-P. Dodelet and G. Wu, *Nat. Catal.*, 2023, **6**, 1215–1227.
14 M. Ogawa, S. Usami, R. Takahama, K. Iwamoto, T. Nabeta, S. Kawashima, R. Kojima, J. Ohyama, T. Hayakawa, Y. Nabae and M. Moriya, *Dalton Trans.*, 2024, **53**, 4426–4431.
15 Y. Meng, J. An, P.-X. Hou, C. Liu and J.-C. Li, *Mater. Chem. Front.*, 2024, **8**, 1927–1949.
16 G. Xing, G. Zhang, B. Wang, M. Tong, C. Tian, L. Wang and H. Fu, *J. Mater. Chem. A*, 2023, **11**, 9493–9503.
17 X. Xie, H. Peng, G. Ma, Z. Lei and Y. Xu, *Mater. Chem. Front.*, 2023, **7**, 2595–2619.
18 X. Dong, W. Zhu and X. Liang, *Dalton Trans.*, 2022, **51**, 12240–12249.
19 Y. Pu, N. Lu, F. Jian, Y. Wang and H. Tang, *Catal. Sci. Technol.*, 2025, **15**, 501–505.
20 Y. Wan, C. Fang, X. Yang, J. Liu and Y. Lin, *J. Mater. Chem. A*, 2024, **12**, 33392–33426.
21 W. Zhang, S. Zhang, P. Guo, H. Chen, Y. Zhou and F. Yu, *J. Colloid Interface Sci.*, 2024, **669**, 896–901.
22 Y. Zhang, J. Feng, C. Ma, X. Gu, L. Yu and L. Dong, *Appl. Surf. Sci.*, 2025, **689**, 162439.
23 W. Liu, D. Rao, J. Bao, L. Xu, Y. Lei and H. Li, *J. Energy Chem.*, 2021, **57**, 428–435.
24 Z. Wang, Z. Sun, K. Li, K. Fan, T. Tian, H. Jiang, H. Jin, A. Li, Y. Tang, Y. Sun, P. W. Wan and Y. Chen, *iScience*, 2024, **27**, 109553.
25 G. Lee, K. Min, S. Cheong, H. Lee, S. E. Shim and S.-H. Baeck, *J. Energy Storage*, 2024, **27**, 109553.
26 S. Zhang, J. Yang, L. Yang, T. Yang, Y. Liu, L. Zhou, Z. Xu, X. Zhou and J. Tang, *Appl. Catal., B*, 2024, **359**, 124485.
27 G. Li, Y. Zheng, H. Guo, Z. Li, G. Zhu, L. Dong, X. Liu and J. Zang, *Int. J. Hydrogen Energy*, 2024, **64**, 468–475.
28 A. N. Eledath and A. Muthukrishnan, *Electrochim. Acta*, 2025, **525**, 146132.
29 S. Cheng, C. Dai, Q. Zhu, H. Gao, Z. Huang, F. Zhang, L. Li, P. Yang and S. Yang, *Appl. Surf. Sci.*, 2025, **688**, 162369.
30 Y. Wang, Y. Chen, Z. Wang, P. Li, J. Zhao, H. Zhao, D. Li, T. He, Y. Wei, Y. Su and C. Xiao, *Int. J. Hydrogen Energy*, 2022, **47**, 18663–18674.
31 Y. Jiang, H. Xu, B. Ma, Z. Zhang and Y. Zhou, *Fuel*, 2024, **366**, 131404.
32 W. Yang, J. Li, L. Lan, Q. Fu, L. Zhang, X. Zhu and Q. Liao, *Int. J. Hydrogen Energy*, 2018, **43**, 8474–8479.